Complementary X-ray and neutron radiography study of the initial lithiation process in lithium-ion batteries containing silicon electrodes[#]

Fu Sun[*1,2], *Henning Markötter*[1,2], *Ingo Manke*[2], *André Hilger*[2], *Saad S. Alrwashdeh*[1,2,3], *Nikolay Kardjilov*[2] *and John Banhart*[1,2]

[1]Institute of Material Science and Technologies
Technical University Berlin
10623 Berlin, Germany
[2]Helmholtz Centre Berlin for Materials and Energy
Hahn-Meitner-Platz 1
14109 Berlin, Germany
[3]Mechanical Engineering Department, Faculty of Engineering
Mu'tah University, P.O Box 7, Al-Karak 61710 Jordan

***Corresponding Author: fu.sun@helmholtz-berlin.de**

[#] manuscript published in: Applied Surface Science 399, 359–366 (2017)
Elsevier, ISSN: 0169-4332 — doi: j.apsusc.2016.12.093

Complementary *in operando* X-ray radiography and neutron radiography measurements were conducted to investigate and visualize the initial lithiation in silicon-electrode lithium-ion batteries. By means of X-ray radiography, a significant volume expansion of Si particles and the Si electrode during the first discharge was observed. In addition, many Si particles were found that never undergo electrochemical reactions. These findings were confirmed by neutron radiography, which, for the first time, showed the process of Li alloying with the Si electrode during initial lithiation. These results demonstrate that complementary X-ray and neutron radiography is a powerful tool to investigate the lithiation mechanisms inside Si-electrode based lithium-ion batteries.

1 Introduction

In operando and nondestructive methods of investigation and visualization are valuable for the study of lithium ion batteries (LIBs), which are believed to meet the future power requirements from consumer electronics to large-scale energy storage systems [1-5]. Previous *in operando* visualizations of LIBs have been realized through several dedicated electrochemical cells with “end/point” contact architecture between the active material [6], and ionic [7] or Li_2O electrolyte [8] as well as with an open-cell configuration [9]. However, these electrochemical cells with the above mentioned features are inherently different from commercially available LIBs [10]. On the other hand, commercial available LIBs have been investigated by *in situ* X-ray diffraction (XRD) [11], nuclear magnetic resonance (NMR) [12] and Raman spectroscopy [13]. Nevertheless, these analytical tools are specialized only in revealing structural and compositional information without imaging ability and therefore do not provide effective spatially resolved information about the underlying de/lithiation mechanism. Obviously, i*n operando* and nondestructive diagnostic techniques with the ability to temporally and spatially visualize de/lithiation processes inside commercially available LIBs might open up new opportunities for high-capacity and high-power electrode materials for next-generation energy storage systems.

In the present work, by using a commercial CR2032 coin cell and a self-made radiography cell (radio-cell, which can adequately simulate a commercial CR2032 coin cell), we investigated and visualized the initial lithiation inside silicon-based LIBs via *in operando* X-ray and neutron radiography measurements. By X-ray radiography, we have observed a significant volume expansion of Si particles and Si electrode during the first discharge. Moreover, we also observed that lots of Si particles never undergo electrochemical reactions. These results were further confirmed by the neutron radiography. In addition, by employing the neutron radiography, for the first time, the process of the Si particles and Si electrode alloying with Li during the first discharge were shown. The obtained results presented here, which cannot be deduced from macroscopic electrochemical characterizations and conventional structure/composition-probing techniques, expand our understanding of the underlying lithiation mechanisms in commercial LIBs and could show the way to new design principles for high-performance next-generation LIBs.

2 Experimental sections

2.1 Materials

Amorphous silicon particles were received from Elkem AS, Norway. Polyvinylidene difluoride (PVDF) binder, carbon black, Celgard separator, CR2032 coin cells and lithium were purchased from MTI Cor. USA. 1M $LiPF_6$ in a volume ratio (1:1) mixture of ethylene carbonate (EC) and dimethyl carbonate (DMC) as well as N-methyl pyrrolidone solvent (NMP) were purchased from Sigma Aldrich. Titanium (Ti) foil was obtained from ANKURO Int. GmbH, Germany. The housing of the X-ray radiography cell ("radio-cell") was made of polyamide-imide (Torlon) from McMaster-Carr Company.

2.2 X-ray radiography cell and CR2032 coin cell

As schematically illustrated in Figure 1B, the *in operando* X-ray radio-cell consists of an upper housing (outer and inner diameters are 25 mm and 8 mm, resp., orange color), a sealing ring (yellow), a lithium plate (8 mm diameter, blue) connected to a copper wire, a separator (8 mm, gray), the Si/carbon electrode (green, cast on a titanium foil, size $2\times2.5\ mm^2$), a titanium foil current collector (length × width is 8 × 6 mm, thickness 5 µm, grey color), an annular copper current collector (outer and inner diameters are 10 mm and 6 mm, resp.) and a lower housing (outer and inner diameters are 25 mm and 12 mm, resp., orange). At the bottom of the lower housing part, two holes were drilled for the copper wire of the lithium plate as well as the wire of the annular copper current collector (not shown in Figure 1B). These two holes were sealed properly during cell assembly.

The composite electrodes for both the X-ray radio-cell and the CR2032 coin cell were made of slurries with weight ratios of Si:carbon black:binder of 75:15:10 in NMP. For the X-ray radio-cell, the slurry was cast onto a 5-µm thick titanium foil. For the CR2032 coin cell, the electrode slurry was directly cast onto the positive casing. Sparsely-coated Si particle slurry was used to facilitate single particle characterization during both X-ray and neutron radiography. The effect of different binders on the electrochemical behavior of Si particles is worth studying in the future. To remove NMP, the material cast onto Ti foil and the coin cell casing were dried in an oven at 60 ℃ for 12 h. Before and after casting, the Ti foil and the CR2032 coin cell casing were weighed to determine the mass of the electrode material. The mass of the Si electrode in the radio-cell was around 1 mg, that of the Si electrode in the CR2032 cell around 1.1 mg. We used commercial 1M $LiPF_6$ in a volume-ratio mixture (1:1) of ethylene carbonate (EC) and dimethyl carbonate (DMC) as electrolyte and the electrolyte

was added to both cells by a syringe. Both cells were assembled in an argon-filled glovebox with humidity and oxygen levels below 0.1 ppm. After assembling these two cells, cyclic voltammetry (CV) was performed in the potential window of 0–2.5 V at a scan rate of 1 $mV \cdot s^{-1}$ in an IviumStat by Ivium Technologies. Then, both cells were galvanostatically discharged during the *in operando* measurements. The discharge capacity and discharge current for both cells were calculated based on Si mass only. The current for the radio-cell was around 0.04 C, that of the CR2032 cell around 0.03 C. The employed different C rates for the CR2032 coin cell and the radio-cell may lead to the different electrochemical results, as shown in Figure 2C and 2D. It has to be noted that the same radio-cell was used for the CV scan and the *in operando* X-ray radiography. Different coin cells were used for the CV scan and the *in operando* neutron radiography.

2.3 *In operando* X-ray radiography and neutron radiography

Both X-ray and neutron radiography were performed at the Helmholtz-Zentrum Berlin, Germany. A schematic representation of the imaging setup is displayed in Figure 1C. For X-ray radiography, an X-ray tube with voltage and current set to 60 kV and 166 µA, respectively, was used. Radiographies were continuously recorded by a flat panel detector (Hamamatsu, C7942SK-05) with a pixel size of 50 µm. Different magnification ratios (given by the distances between X-ray source, sample and detector) were chosen to provide a varied spatial resolution [14]. In the present paper, the source-to-object distance (SOD) was 58 mm, the source-to-detector distance (SDD) 500 mm. Thus one pixel represents 5.76 µm of the sample.

Neutron radiography was carried out at the V7/CONRAD beamline at the BER II reactor [15]. The beamline provides neutrons with wavelengths between 2 and 6 Å with a maximum at 3 Å. The conical beam geometry is shaped by a pinhole placed at a distance of 5 m in front of the CR2032 coin cell. The detector system was based on a CCD camera integrated in a light-tight box comprising a scintillator screen and a lens system projecting the image from the scintillator via a mirror onto the CCD chip. The 16 bit CCD camera used (Andor DW-436N-BV) has a Peltier-cooled chip with 2048 × 2048 pixels. The spatial resolution achieved was 6.43 µm.

2.4 Underlying principle of X-ray and neutron imaging

Radiography with X-rays and neutrons is based on the attenuation of rays by the atoms of a sample and is determined by their respective scattering and absorption cross-sections as governed by the Beer-Lambert law, $I = I_0(\lambda)e^{-\mu(\lambda)d}$, where, I_0 and I are the incident and transmitted beam intensities for a given wavelength λ, μ is the attenuation coefficient and d is the thickness of the sample [16]. SI (Supporting Information) Figure 1A shows the mass-specific attenuation coefficient μ_m, i. e. the linear coefficient μ over the density ρ of an element, given as a function of the atomic number for all the elements from Z = 1 to Z = 92 [16]. The values displayed as blue line in SI Figure 1A refer to X-rays of 100 keV energy. Clearly, μ_m varies smoothly with increasing Z. This is because X-rays interact with the electronic shell, as shown in SI Figure 1B, and the interaction cross-section increases with the number of electrons, i.e. with atomic number [17]. SI Figure 1A further shows the mass attenuation coefficients for thermal neutrons (25 meV neutron energy, red dots) as a function of Z. Here, the trend is much less regular. The reason for this is that unlike X-rays neutrons interact directly with the atomic nucleus as illustrated in SI Figure 1B and this interaction depends on the internal configuration of a nucleus. While X-rays have higher interaction cross sections with Si (Z = 14) than with Li (Z = 3) and C (Z=6), neutrons interact stronger with Li than with Si and C. It has also to be noted that we have used titanium foil as the current

collector instead of copper foil although titanium possesses a relatively lower conductivity. The reason is that titanium has a lower X-ray absorption compared with copper, which guarantees a better X-ray imaging. A quantitative comparison of the linear attenuation coefficients for X-rays and neutrons is shown in SI Figure 2. Specifically, the X-ray attenuation coefficients for Si and $Li_{4.4}Si$ are calculated to be 2.15 (cm^{-1}) and 0.87 (cm^{-1}) [18]. The neutron absorption coefficients for Si and $Li_{4.4}Si$ are calculated to be 0.017 (cm^{-1}) and 7.372 (cm^{-1}) [19].

Considering the different interactions between X-rays and neutrons with the elements Si, C and Li, we built a custom-made plastic radiography cell ("radio-cell") for X-ray radiography to directly observe the morphological changes of the Si electrode. We use a self-assembled commercial CR2032 coin cell for neutron radiography (because the easy neutron penetration through the steel casing) to directly visualize Si-Li alloying during the first discharge step.

2.5 Data processing

Both radiography datasets were processed with ImageJ. For the *in operando* X-ray radiography movie, 18 images were combined with a median filter in order to reduce the noise level. For in operando neutron radiography, 25 images were used in that way. More information concerning image processing is in given in the SI.

3 Results and discussion

A schematic illustration and a photograph of the self-made radio-cell are given in Figure 1, along with a schematic representation of the imaging setup (both for micro X-ray radiography and neutron radiography). The self-assembled CR2032 coin cell was used for the *in operando* neutron radiography. The radio-cell is used for *in operando* X-ray radiography. Both cells contain a distribution of Si particles ranging from 125 to 180 µm diameter [20]. The cyclic voltammetry (CV) scans of both cells are displayed in Figure 2. The broad cathodic peak at around 1.0 V for both radio-cell and coin cell, as well as the cathodic peak at 2.0 V for radio-cell are intimately related to the side electrolyte decomposition of forming the solid electrolyte interface (SEI) during first cathodic scan [21]. A characteristic cathodic peak at around 0 V is suggestive of alloy formation of Li with Si [22]. During the following anodic scan, the anodic peaks at around 0.4 V and 1.0 V can be attributed respectively to the Li-Si de-alloying reaction and the oxidation reaction of byproduct compounds reduced at cathodic process [23]. The cells were characterized by X-ray radiography and neutron radiography during discharge. The resulting discharge curves are also shown in Figure 2.

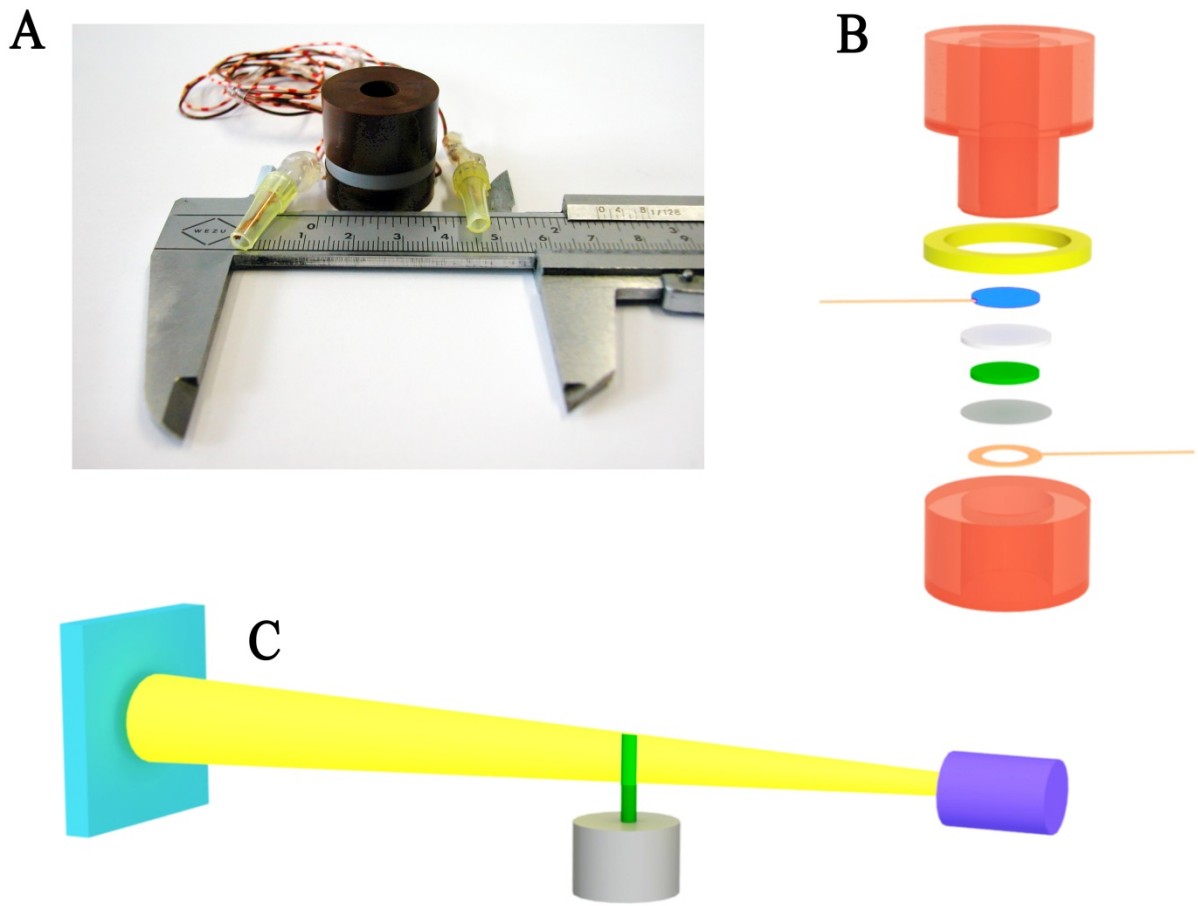

Figure 1 A, Photograph of the *in operando* X-ray radio-cell, B, Schematic illustration of the radio-cell as explained in the experimental section, C, Schematic representation of the experimental setup. From right to left: X-ray source (purple), beam (yellow), sample and sample table (green and gray), detector (blue). The neutron radiography setup is designed analogously. In both setups, the samples (X-ray radio-cell and neutron CR2032 coin cell) were penetrated by the x-rays and neutrons along their axes.

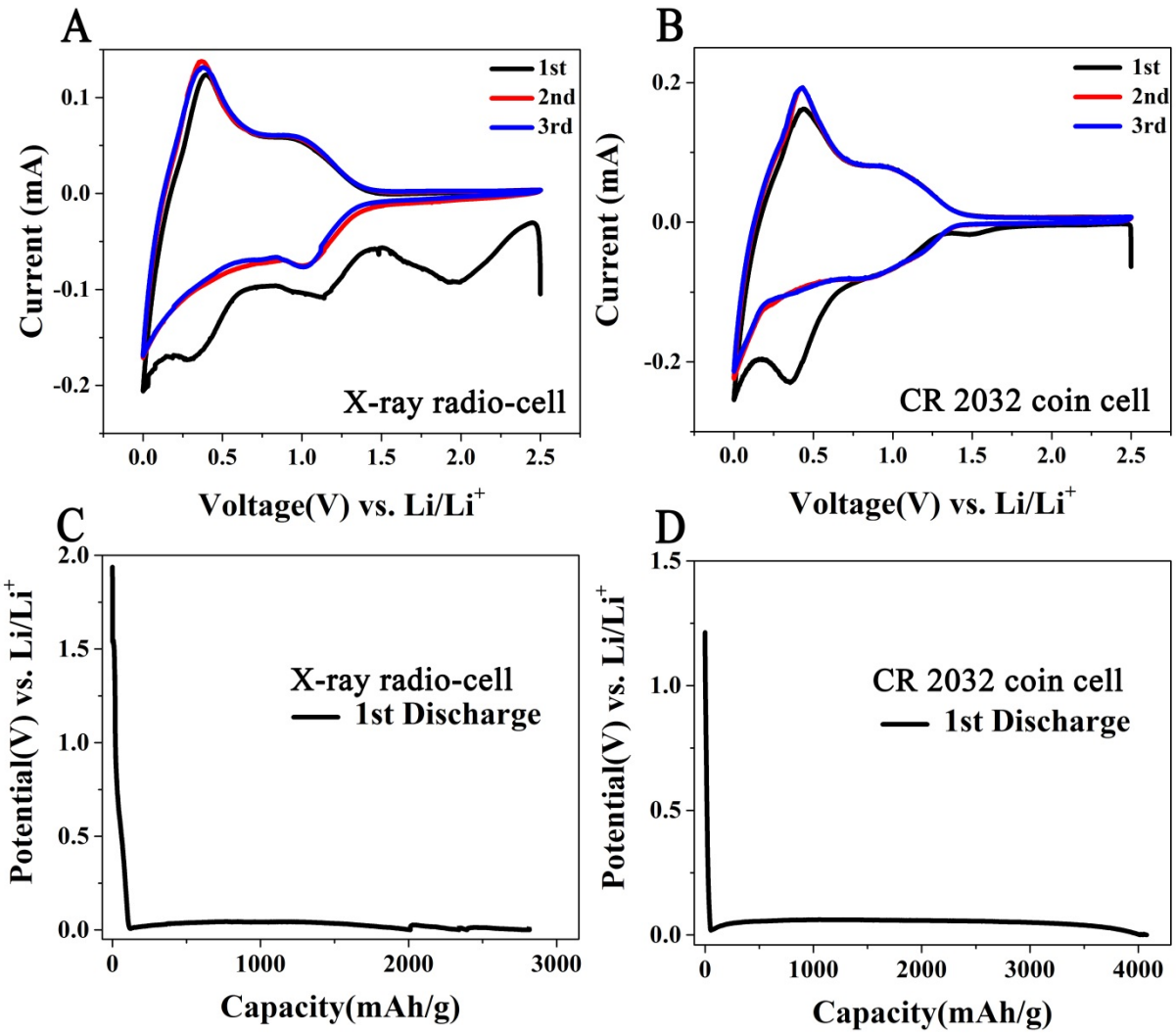

Figure 2 Electrochemical characterizations of the two types of cells used: A and B, CV scans of the radio-cell and CR2032 cell; C and D, first discharge curves of the radio-cell and CR2032 cell. Figure A and C are revised with permission from ref. 28.

Overviews of the pristine state of the radio-cell and the CR2032 coin cell are displayed in Figure 3. The complete *in operando* investigations of discharge processes are presented in Supporting Movies (SMs). Figure 4 displays snapshots of the first discharge of the radio-cell during *in operando* X-ray radiography, Figure 5 the results obtained during the first discharge of the CR2032 coin cell by *in operando* neutron radiography.

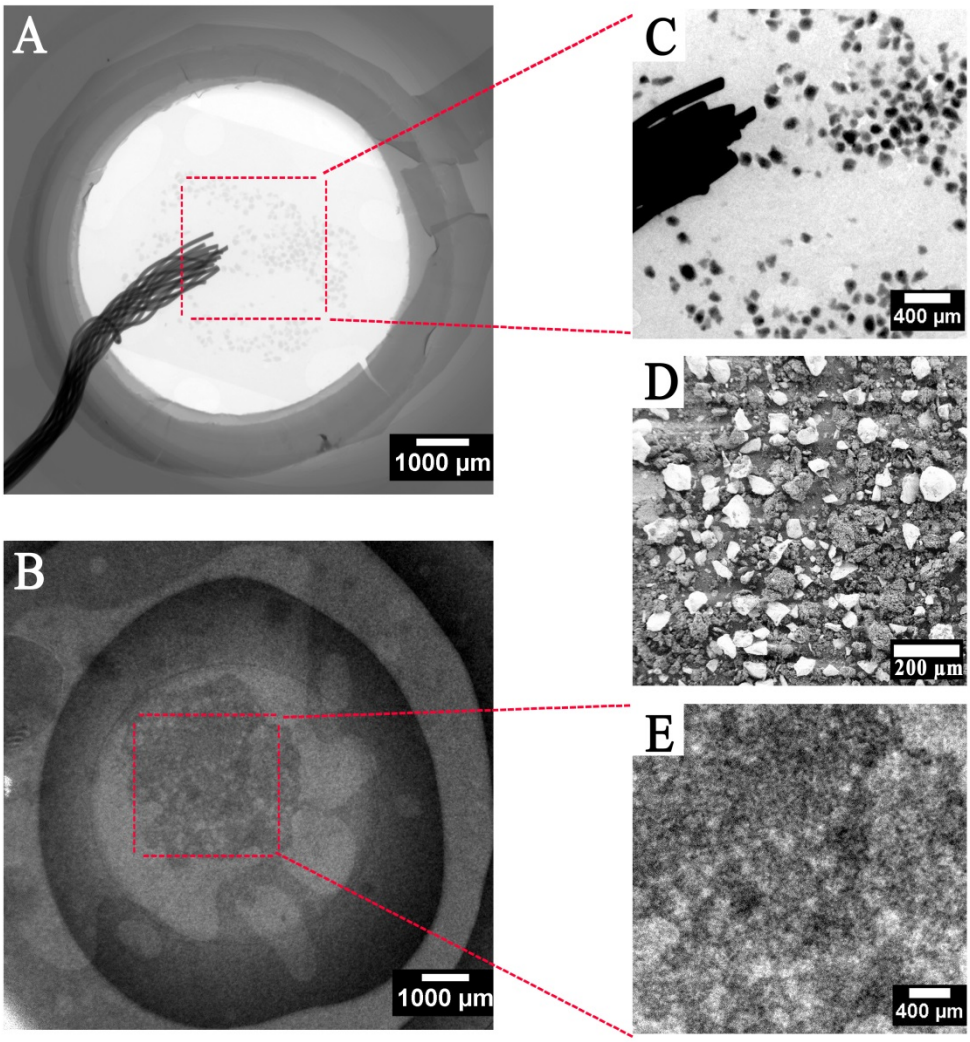

Figure 3 Overviews of the pristine state of the radio-cell (A) and CR2032 cell (B). In A, due to the low X-ray absorption of the plastic housing, lithium and separator, only the copper wire, the annular copper current collector and Si particles are visible. In B, materials with different neutron absorptions become visible as the neutrons pass through the coin cell materials. C, the enlarged part showing Si particles (black spots) as marked in A. E, enlarged part showing Si particles (white spots) as marked in B. D, Scanning electron microscopy (SEM) image taken using a Zeiss ultraplus microscope to show the typical particle shape found in the materials visualized by X-ray and neutron radiography.

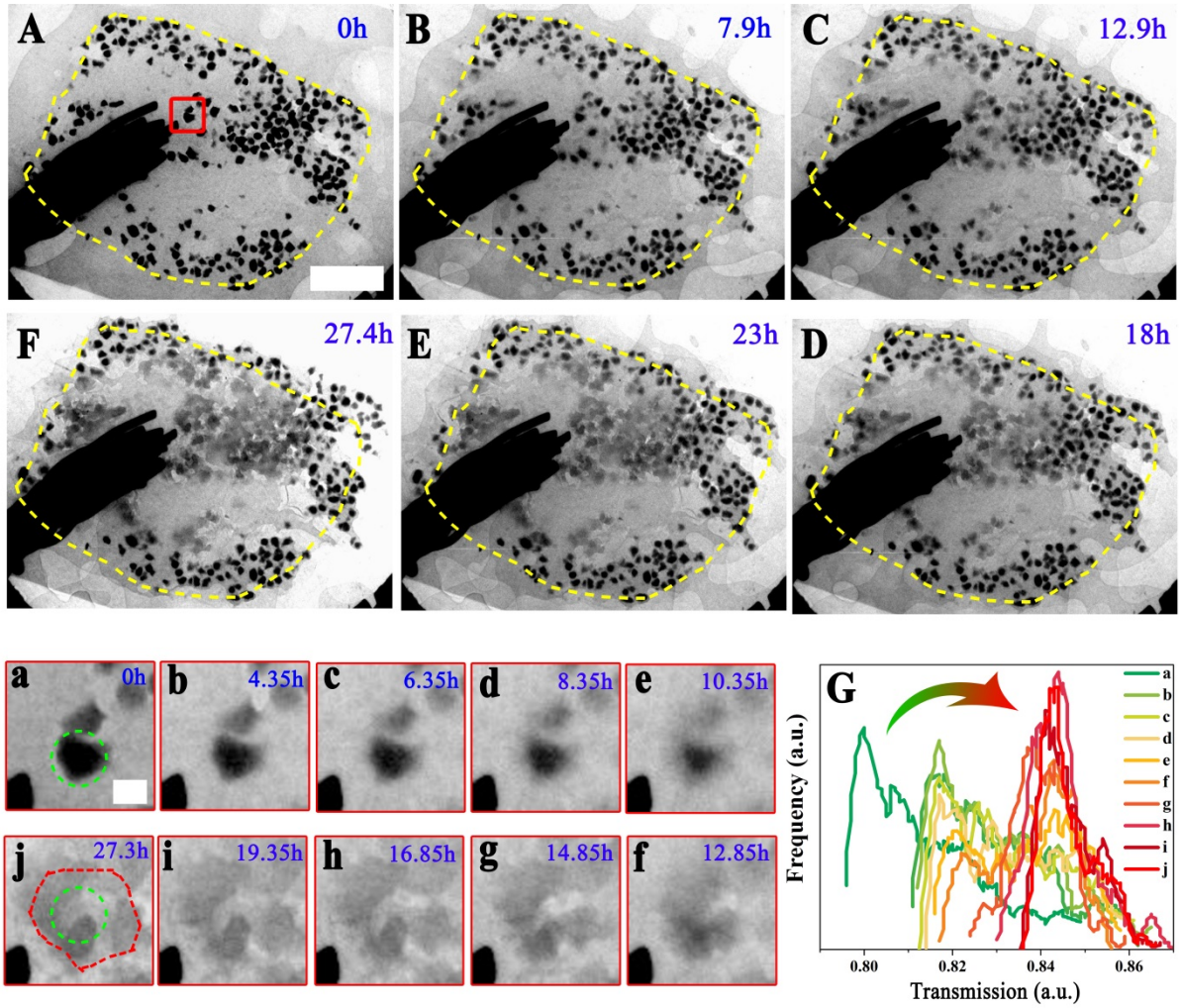

Figure 4 Snapshots from the *in operando* X-ray radiography sequence acquired during the first discharge. The letters from A to F refer to elapsing time (see also the time lable). The region encircled in yellow is the original area that has covered the electrode; from a to j, different states of the Si particles during first lithiation as marked by the red rectangle in A; G, histogram of the Si particle in green circle in a as a function of discharge state. The arrow implies the transformation from a lower transmission to a higher transmission. The length of the scale bar in A is 1 mm, that in a 100 µm. Revised with permission from ref. 28. More information is in SI.

As can be seen from the *in operando* X-ray radiography in Figure 4, there is a volume expansion of the Si electrode during the first discharge. We tracked the particles enclosed by the red rectangle to investigate the morphological changes of individual Si particles during initial lithiation. From Figure 4a to 4j, the surface of the Si particles appears increasingly blurred and the well-known "core-shell" model reaction can be observed: during the discharge process, it is the shell of this particle that undergoes lithiation first (evidenced by the blurred contour) while the core remains un-changed. During further discharge, the lithiation front moves gradually from the shell to the core (evidenced by a growing gray Li_xSi shell and a shrinking dark Si core) as a function of lithiation state [24]. Comparing the pristine (green circle in Figure 4a) with the fully lithiated state (red circle in Figure 4j) of the Si particle, it is estimated that the diameter increased by as much as 130% during the first lithiation. More direct evidence for Li alloying into Si is given by the change of the X-ray transmission of the area containing just the particle as shown in Figure 4G, in which the leftmost peak can be attributed to the Si particle. Following the first lithiation, the Si peak increasingly moves to the right, implying that the Si particle is gradually transforming from the high-density Si

phase to a lower-density Li_xSi phase ($1<x<4.4$) [25]. The results are in good agreement with previous ones [26]. However, we have also observed that many Si particles never undergo alloying during the first discharge, i.e. they are electrochemically inactive during the macroscopic discharge process on the battery level. Such particles are shown in the outer region in Figure 4A to 4F and appear dark throughout lithiation. Considering that the applied external current concentrates only on the electrochemically active particles [10], the presence of these electrochemically inactive Si particles explains the experimentally observed discrepancy between global electrochemical measurements and local spectroscopic data [27-30]. More specific experiments aimed at clarifying the reasons of the inhomogeneous reaction are desirable.

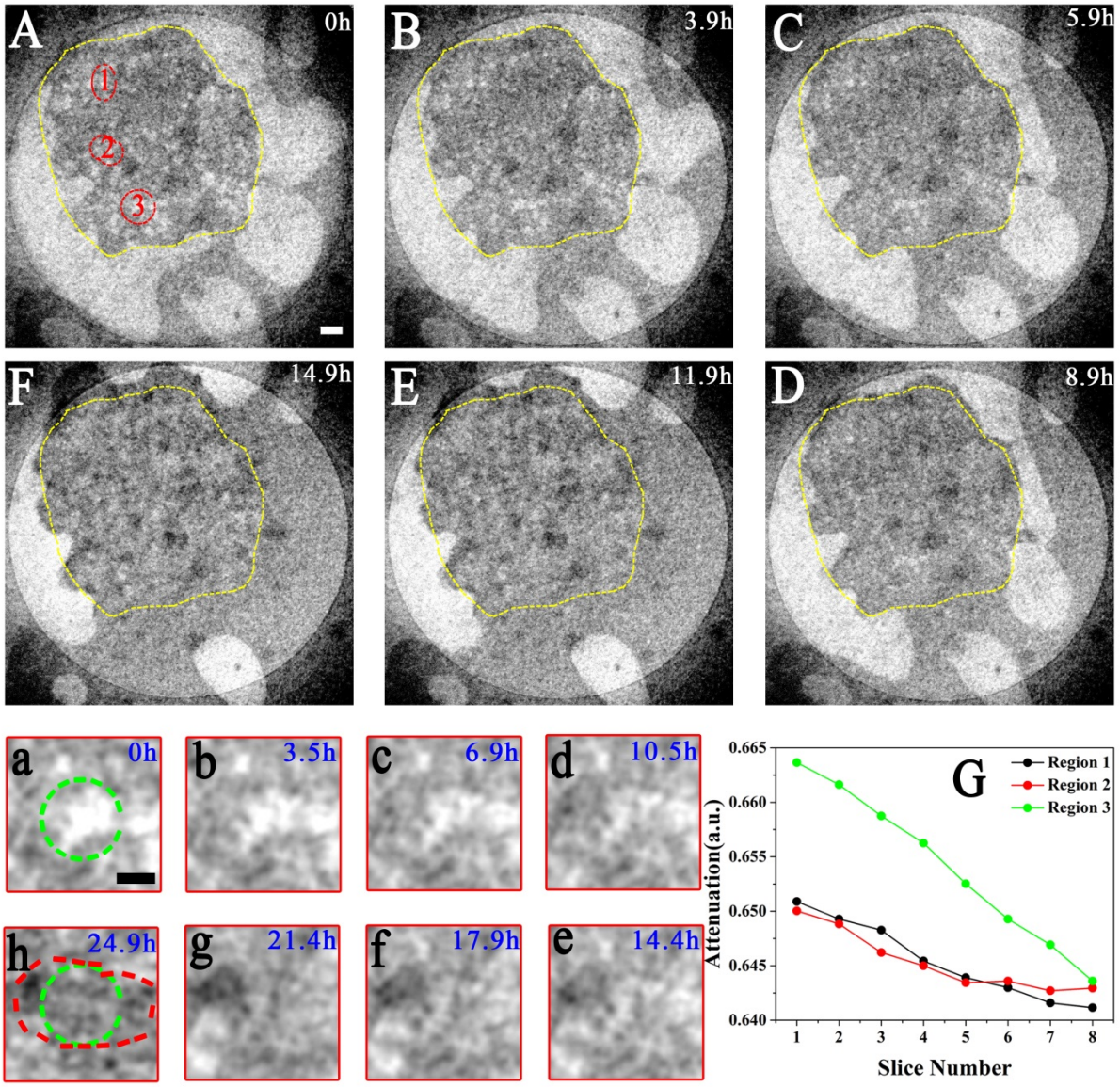

Figure 5 Snapshots from an *in operando* neutron radiography series taken during the first discharge: The sequence of letters from A to F refers to elapsing time (see also the time label). The region encircled in yellow is the original area that covers the initial electrode; from a to h, different states of the Si particle during first lithiation as marked in the 3rd red circular region in A, G, attenuation changes of regions 1, 2 and 3 defined in A as a function of slice number (discharge time). Note that the values in G are the relative change of the neutron attenuation coefficient. The scale bar in A is 400 µm, the scale bar in a 200 µm long. More information is in SI.

Snapshots of a series of neutron radiographies taken *in operando* are shown in Figure 5. Here, Si particles appear white and the Si electrode gray because of the presence of carbon and electrolyte. The white region surrounding the Si electrode contains generated gas. Following the first discharge, we can clearly discern the gas movement and the electrolyte displacement driven by the generated gases. The results are in good agreement with previous observations [31-33]. Moreover, similar to the results of X-ray radiography, we can also observe an expansion of the Si electrode during the first lithiation. Furthermore, it follows from Figure 5a to 5h that during first lithiation the white Si particles gradually turn gray and finally, at the end of lithiation, dark. The reason is that a high density of lithium ions, flowing from lithium electrode or electrolyte during the first discharge, will alloy with Si with electrons from the current collector [34] and this large accumulation of lithium markedly increases the absorption of neutrons. A more direct evidence for the alloying of Si is given by changes of the neutron transmission as shown in Figure 5G. The transmission of neutrons through three different regions decreases gradually as a function of discharge time.

The detailed volume expansion process of Si particle during lithiation is characterized by complementary *in operando* X-ray and neutron radiography. As clearly observed from Figure 4a to Figure 4j, the lithiation starts by lithiating the surface of Si particle (evidenced by the emerged blurry contour of Si particle) due to that the surface diffusion of Li atoms is very fast compared to bulk lithiation [35]. This growing Li_xSi shell surrounds a shrinking unlithiated Si core, forming the well-known "core-shell" model reaction. During further discharge, the accumulation of Li and the associated addition of electron density to the core Si framework will continue to weaken the Si network, resulting in Si-Si bond brakeage and the formation of Li_xSi alloy [36]. The lithiation process can be clearly observed from the X-ray radiography results: the blurred gray Li_xSi alloy shell gradually grows at the expense of the dark unlithiated Si core during lithiation, accompanying this process is the significant volume expansion of Si particle. This process is further demonstrated by the neutron radiography, as shown in Figure 5a to Figure 5h: the original white Si particle gradually becomes gray and finally dark gray due to the formation of Li_xSi alloy. The accompanying volume expansion is also observed between the pristine white Si particle (green circle in Figure 5h) and the lithiated dark gray Li_xSi alloy (red circle in Figure 5h).

This is the first time that Li alloying with a Si electrode during the first lithiation is investigated and visualized by neutron radiography. In addition, similar to what results from X-ray radiography, we have also observed that some Si particles (white spots) are electrochemically inactive throughout discharge. The currently observed electrochemically inactive electrode particles agrees well with previously reported heterogeneous de/lithiation among multiple electrode particles [37]. It has been suggested that the inhomogeneous contact between the active electrode particles and the conductive/binder agents, as well as the different C rates subjected to the cell may result in the observed heterogeneous lithiation process [10]. Resultantly, the complex electrode structure and the complicated morphology and conditions with respect to porosity, tortuosity, conductivity and percolation ability for the electrolyte may lead to inhomogeneous electrochemical reactions among ensemble active particles. The currently observed inactive Si particles cannot be characterized from conventional electrochemical characterizations and are believed to decrease the energy density of the cell. This result implies that future work in optimizing the entire electrode architecture that involve all electrode materials ionically and electronically connected to electrolyte and electric conducting network is highly desired.

4 Conclusions

Complementary *in operando* X-ray radiography and neutron radiography measurements were conducted to investigate and visualize the lithiation process in Si-anode lithium-ion batteries. For neutron radiography, a self-assembled commercial CR2032 coin cell was used. For X-ray radiography, a radiography-cell, which can adequately simulate the commercial CR2032 coin cell was designed and prepared. By X-ray radiography, a significant volume expansion of the Si particles and Si electrode during the first lithiation were observed. In addition, many Si particles were found that never undergo electrochemical reactions. These findings were confirmed by neutron radiography, which showed the process of lithiation of a Si electrode for the first time. These results also demonstrate that complementary X-ray and neutron radiography measurements are powerful investigation tools to study the lithiation mechanisms in Si-anode lithium-ion batteries. Investigations of the effects of different cycling rates and a quantitative analysis of lithium alloying kinetics should be carried out in the future.

Acknowledgements

We thank Norbert Beck for fabricating the radiography battery and Elkem AS for providing silicon particles. This work was sponsored by the Helmholtz-Zentrum Berlin and the China Scholarship Council.

References

[1] D.X. Liu, J. Wang, K. Pan, J. Qiu, M. Canova, L.R. Cao, A.C. Co, In situ quantification and visualization of lithium transport with neutrons, Angew. Chem. Int. Ed. 53 (2014) 9498-9502.

[2] F. Sun, K. Huang, X. Qi, T. Gao, Y. Liu, X. Zou, X. Wei, J. Zhong, A rationally designed composite of alternating strata of si nanoparticles and graphene: A high-performance lithium-ion battery anode, Nanoscale 5 (2013) 8586-8592.

[3] F. Sun, K. Huang, X. Qi, T. Gao, Y. Liu, X. Zou, J. Zhong, Enhanced 3d hierarchical double porous co3o4/graphene architecture for superior rechargeable lithium ion battery, Ceram. Int. 40 (2014) 2523-2528.

[4] Y. Liu, K. Huang, Y. Fan, Q. Zhang, F. Sun, T. Gao, Z. Wang, J. Zhong, Binder-free si nanoparticles@carbon nanofiber fabric as energy storage material, Electrochim. Acta 102 (2013) 246-251.

[5] F. Sun, K. Huang, Y. Liu, T. Gao, Y. Han, J. Zhong, Hierarchical structure of co3o4 nanoparticles on si nanowires array films for lithium-ion battery applications, Appl. Surf. Sci. 266 (2013) 300-305.

[6] J.Y. Huang, L. Zhong, C.M. Wang, J.P. Sullivan, W. Xu, L.Q. Zhang, S.X. Mao, N.S. Hudak, X.H. Liu, A. Subramanian, H. Fan, L. Qi, A. Kushima, J. Li, In situ observation of the electrochemical lithiation of a single sno2 nanowire electrode, Science 330 (2010) 1515-1520.

[7] M. Gu, Y. Li, X. Li, S. Hu, X. Zhang, W. Xu, S. Thevuthasan, D.R. Baer, J.-G. Zhang, J. Liu, C. Wang, In situ tem study of lithiation behavior of silicon nanoparticles attached to and embedded in a carbon matrix, ACS Nano 6 (2012) 8439-8447.

[8] X.H. Liu, J.W. Wang, S. Huang, F. Fan, X. Huang, Y. Liu, S. Krylyuk, J. Yoo, S.A. Dayeh, A.V. Davydov, S.X. Mao, S.T. Picraux, S. Zhang, J. Li, T. Zhu, J.Y. Huang, In situ atomic-scale imaging of electrochemical lithiation in silicon, Nat Nano 7 (2012) 749-756.

[9] L. Zhong, X.H. Liu, G.F. Wang, S.X. Mao, J.Y. Huang, Multiple-stripe lithiation mechanism of individual sno_2 nanowires in a flooding geometry, Phys. Rev. Lett. 106 (2011) 248302-248305.

[10] Y. Li, F. El Gabaly, T.R. Ferguson, R.B. Smith, N.C. Bartelt, J.D. Sugar, K.R. Fenton, D.A. Cogswell, A.L.D. Kilcoyne, T. Tyliszczak, M.Z. Bazant, W.C. Chueh, Current-induced transition from particle-by-particle to concurrent intercalation in phase-separating battery electrodes, Nat Mater 13 (2014) 1149-1156.

[11] S. Misra, N. Liu, J. Nelson, S.S. Hong, Y. Cui, M.F. Toney, In situ x-ray diffraction studies of (de)lithiation mechanism in silicon nanowire anodes, ACS Nano 6 (2012) 5465-5473.

[12] K. Ogata, E. Salager, C.J. Kerr, A.E. Fraser, C. Ducati, A.J. Morris, S. Hofmann, C.P. Grey, Revealing lithium–silicide phase transformations in nano-structured silicon-based lithium ion batteries via in situ nmr spectroscopy, Nat Commun 5 (2014) 3217-3227.

[13] S. Ramdon, B. Bhushan, S.C. Nagpure, In situ electrochemical studies of lithium-ion battery cathodes using atomic force microscopy, J. Power Sources 249 (2014) 373-384.

[14] R. Triolo, G. Giambona, F. Lo Celso, I. Ruffo, N. Kardjilov, A. Hilger, I. Manke, A. Paulke, Combined application of x-ray and neutron imaging techniques to wood materials, Conserv. Sci. Cult. Herit. 10 (2010) 143-158.

[15] N. Kardjilov, A. Hilger, I. Manke, A. Griesche, J. Banhart, Imaging with cold neutrons at the conrad-2 facility, Phys. Procedia. 69 (2015) 60-66.

[16] J. Banhart, A. Borbély, K. Dzieciol, F. Garcia-Moreno, I. Manke, N. Kardjilov, A.R. Kaysser-Pyzalla, M. Strobl, W. Treimer, X-ray and neutron imaging – complementary techniques for materials science and engineering, Int. J. Mater. Res. 101 (2010) 1069-1079.

[17] M. Strobl, I. Manke, N. Kardjilov, A. Hilger, M. Dawson, J. Banhart, Advances in neutron radiography and tomography, J. Phys. D: Appl. Phys. 42 (2009) 243001-243021.

[18] http://henke.lbl.gov/optical_constants/, X-ray link.

[19] https://www.ncnr.nist.gov/instruments/bt1/neutron.html, Neutron link.

[20] C. Wang, H. Wu, Z. Chen, M.T. McDowell, Y. Cui, Z. Bao, Self-healing chemistry enables the stable operation of silicon microparticle anodes for high-energy lithium-ion batteries, Nat Chem 5 (2013) 1042-1048.

[21] Ó. Vargas, Á. Caballero, J. Morales, E. Rodríguez-Castellón, Contribution to the understanding of capacity fading in graphene nanosheets acting as an anode in full li-ion batteries, Acs Appl. Mater. Interfaces 6 (2014) 3290-3298.

[22] Y.S. Kim, K.W. Kim, D. Cho, N.S. Hansen, J. Lee, Y.L. Joo, Silicon-rich carbon hybrid nanofibers from water-based spinning: The synergy between silicon and carbon for li-ion battery anode application, ChemElectroChem 1 (2014) 220-226.

[23] C. Pereira-Nabais, J. Światowska, A. Chagnes, F. Ozanam, A. Gohier, P. Tran-Van, C.-S. Cojocaru, M. Cassir, P. Marcus, Interphase chemistry of si electrodes used as anodes in li-ion batteries, Appl. Surf. Sci. 266 (2013) 5-16.

[24] J.M. Yuk, H.K. Seo, J.W. Choi, J.Y. Lee, Anisotropic lithiation onset in silicon nanoparticle anode revealed by in situ graphene liquid cell electron microscopy, ACS Nano 8 (2014) 7478-7485.

[25] J. Gonzalez, K. Sun, M. Huang, J. Lambros, S. Dillon, I. Chasiotis, Three dimensional studies of particle failure in silicon based composite electrodes for lithium ion batteries, J. Power Sources 269 (2014) 334-343.

[26] X.H. Liu, L. Zhong, S. Huang, S.X. Mao, T. Zhu, J.Y. Huang, Size-dependent fracture of silicon nanoparticles during lithiation, ACS Nano 6 (2012) 1522-1531.

[27] G. Brunetti, D. Robert, P. Bayle-Guillemaud, J.L. Rouvière, E.F. Rauch, J.F. Martin, J.F. Colin, F. Bertin, C. Cayron, Confirmation of the domino-cascade model by lifepo4/fepo4 precession electron diffraction, Chem. Mater. 23 (2011) 4515-4524.

[28] F. Sun, H. Markötter, K. Dong, I. Manke, A. Hilger, N. Kardjilov, J. Banhart, Investigation of failure mechanisms in silicon based half cells during the first cycle by micro x-ray tomography and radiography, J. Power Sources 321 (2016) 174-184.

[29] F. Sun, H. Markötter, D. Zhou, S.S.S. Alrwashdeh, A. Hilger, N. Kardjilov, I. Manke, J. Banhart, In situ radiographic investigation of (de)lithiation mechanisms in a tin-electrode lithium-ion battery, ChemSusChem 9 (2016) 946-950.

[30] L. Zielke, F. Sun, H. Markötter, A. Hilger, R. Moroni, R. Zengerle, S. Thiele, J. Banhart, I. Manke, Synchrotron x-ray tomographic study of a silicon electrode before and after discharge and the effect of cavities on particle fracturing, ChemElectroChem 3 (2016) 1170-1177.

[31] D. Goers, M. Holzapfel, W. Scheifele, E. Lehmann, P. Vontobel, P. Novák, In situ neutron radiography of lithium-ion batteries: The gas evolution on graphite electrodes during the charging, J. Power Sources 130 (2004) 221-226.

[32] M. Lanz, E. Lehmann, R. Imhof, I. Exnar, P. Novák, In situ neutron radiography of lithium-ion batteries during charge/discharge cycling, J. Power Sources 101 (2001) 177-181.

[33] F. Sun, H. Markötter, I. Manke, A. Hilger, N. Kardjilov, J. Banhart, Three-dimensional visualization of gas evolution and channel formation inside a lithium-ion battery, Acs Appl. Mater. Interfaces 8 (2016) 7156-7164.

[34] G. Chen, T.J. Richardson, Continuity and performance in composite electrodes, J. Power Sources 195 (2010) 5387-5390.

[35] M.T. McDowell, I. Ryu, S.W. Lee, C. Wang, W.D. Nix, Y. Cui, Studying the kinetics of crystalline silicon nanoparticle lithiation with in situ transmission electron microscopy, Adv. Mater. 24 (2012) 6034-6041.

[36] B. Key, M. Morcrette, J.-M. Tarascon, C.P. Grey, Pair distribution function analysis and solid state nmr studies of silicon electrodes for lithium ion batteries: Understanding the (de)lithiation mechanisms, J. Am. Chem. Soc. 133 (2011) 503-512.

[37] W.C. Chueh, F. El Gabaly, J.D. Sugar, N.C. Bartelt, A.H. McDaniel, K.R. Fenton, K.R. Zavadil, T. Tyliszczak, W. Lai, K.F. McCarty, Intercalation pathway in many-particle lifepo4 electrode revealed by nanoscale state-of-charge mapping, Nano Lett. 13 (2013) 866-872.